Sakthi Kumar Arul Prakash
Department of Mechanical Engineering,
Carnegie Mellon University,
Pittsburgh, PA 15213
e-mail: sarulpra@andrew.cmu.edu

Tobias Mahan
Department of Mechanical Engineering,
The Pennsylvania State University,
University Park, PA 16802
e-mail: tjm450@psu.edu

Glen Williams
Department of Mechanical Engineering,
The Pennsylvania State University,
University Park, PA 16802
e-mail: gtw5020@psu.edu

Christopher McComb
SEDTAPP,
The Pennsylvania State University,
University Park, PA 16802
e-mail: mccomb@psu.edu

Jessica Menold
Department of Mechanical Engineering,
SEDTAPP,
The Pennsylvania State University,
University Park, PA 16802
e-mail: jdm5407@psu.edu

Conrad S. Tucker
Department of Mechanical Engineering,
Carnegie Mellon University,
Pittsburgh, PA 15213
e-mail: conradt@andrew.cmu.edu

Detection of System Compromise in Additive Manufacturing Using Video Motion Magnification

Three-dimensional printing systems have expanded the access to low cost, rapid methods for attaining physical prototypes or products. However, a cyber attack, system error, or operator error on a 3D-printing system may result in catastrophic situations, ranging from complete product failure, to small types of defects which weaken the structural integrity of the product. Such defects can be introduced early-on via solid models or through G-codes for printer movements at a later stage. Previous works have studied the use of image classifiers to predict defects in real-time and offline. However, a major restriction in the functionality of these methods is the availability of a dataset capturing diverse attacks on printed entities or the printing process. This paper introduces an image processing technique that analyzes the amplitude and phase variations of the print head platform arising through induced system manipulations. The method uses an image sequence of the printing process to perform an offline spatio-temporal video decomposition to amplify changes attributable to a change in system parameters. The authors hypothesize that a change in the amplitude envelope and instantaneous phase response as a result of a change in the end-effector translational instructions to be correlated with an AM system compromise. Two case studies are presented, one verifies the hypothesis with statistical evidence in support of the method while the other studies the effectiveness of a conventional tensile test to identify system compromise. The method has the potential to enhance the robustness of cyber-physical systems such as 3D printers. [DOI: 10.1115/1.4045547]

Keywords: computer vision for additive manufacturing, video magnification, structural analysis, cyber-security for 3D printing

1 Introduction

Additive manufacturing systems are becoming increasingly interconnected. However, this interconnectivity adds risk to the manufacturing system, as vital processes are left exposed to hackers. Cyber-physical production systems have already been the target of attacks [1], as seen in the destruction of several processing centrifuges by the Stuxnet worm. By targeting specific machines, the virus reduced manufacturing capability and led to dangerous catastrophic failures in uranium enrichment centers. While additive manufacturing systems have only recently become a method for the production of critical, structural components, they present a valuable target for anyone hoping to disrupt the manufacture of safe, reliable goods.

Introduction of defects into a digital part, either through operator error or system error, may affect the structural integrity and hence the print quality of critical components [2]. Additionally, defects can also be introduced by failing to fill certain spatial locations thereby leading to void or crack formation. A straight-forward approach at solving the problem of defect recognition can be solved by training an image classifier with images of defects or by learning kernels from texture analysis [3,4]. However, these methods are at a disadvantage due to a requirement in large scale diverse data requirement and annotations that may not be available for every possible scenario.

By amplifying imperceptible color changes in human skin as a result of a change in blood volume flow [5], researchers in the biomedical optics space have been able to find bio-markers such as heart rate [6] and respiratory rate [7]. We hypothesize that by using a similar approach in detecting spatio-temporal changes in an AM printing process, the changes in phase and amplitude identified by an off-the-shelf camera can be correlated with a compromised system. A compromise in system utility is meaningful with a comparison between two different system states, wherein one of which is assumed to represent the uncompromised state.

In this work, the definition of AM hack will be limited to a single defect type, namely a void defect with varying depth using only the filament freeform fabrication method. To make a case for studying system compromise in AM as a result of CAD-induced defects and to show that a defect as simple as a void is able to bypass existing tools, we conduct the following case study. We use PTC CREO 3.0 [8], a commonly used design software in the automotive and aerospace industries and use the software provided geometrical model comparison tool to compare an uncompromised CAD model with a compromised CAD model with the same defect sizes and type as explained later in the paper. We find that when the distance between spacing to compare is set to the lowest possible value and the tolerance varied depending on the thickness of the induced void, the software was unable to detect a void if the tolerance was even slightly larger than the size of the void. In the case of multiple voids or multiple defects of varying sizes, it becomes difficult to set the right tolerance value or alternatively since the AM manufacturing

Contributed by the Design for Manufacturing Committee of ASME for publication in the JOURNAL OF MECHANICAL DESIGN. Manuscript received June 14, 2019; final manuscript received October 27, 2019; published online November 26, 2019. Assoc. Editor: Carolyn Seepersad.

workflow can be hacked [9,10], it is likely that the tolerance be changed to allow the system to approve the model for printing.

Our method aims to identify and differentiate between defect magnitudes via changes in the properties of the image sequence, as induced by the end effector tool path movements. This section provides an introduction and motivation for this work. Section 2 highlights cyber-security attacks in AM, further reinforcing the need for predictive technologies while the latter sub-sections focus on related work, their limitations and the research questions we tackle in this paper. Section 3 introduces the method of phase-based video amplification in the context of AM and feature extraction from the resulting high-dimensional data to further perform classification. Section 4 briefly elucidates data collection, experimental, and validation set-up, while Sec. 5 discusses the results as obtained from statistical analysis followed by conclusion to the study.

2 Literature Review

2.1 Cyber-Security Attacks in Additive Manufacturing. The interconnectivity and flexibility of AM systems [11,12] creates opportunities for hackers to steal, alter, or delete designs [13], as well as prevent normal and safe operation of machinery [14]. This can cost manufacturers considerably [15], as any loss of productivity or intellectual property could disrupt revenue streams.

A number of controlled laboratory experiments have demonstrated possible attacks on additive manufacturing systems. These attacks typically fall into one of three categories: data siphoning/exfiltration [16–18], denial of service [10,19], and defect introduction [20]. While each poses a real threat to manufacturing, the most well studied is likely data siphoning/exfiltration.

Cyber-security measures have been suggested to prevent data siphoning from additive manufacturing systems. Groups like Chen et al. [21] and Gupta et al. [22] embedded features in CAD models to ensure that parts could only be produced with predetermined settings, thus limiting access to the original designers. Fadhel et al. [23] created a method of applying a digital and physical signature to parts, embedding evidence of ownership directly into the object. With these measures, specific applications can be protected against siphoning attacks. In addition to data siphoning of the design files, hackers can gather a variety of peripheral information from additive manufacturing systems, such as sound [24], reflected light [17], and radiant heat [25], that are collectively known as "side-channels." Hackers could use these side channels to steal intellectual property or other confidential processes from manufacturers. Fortunately, system administrators can also use these side-channels to detect malicious attacks [26]. Beyond intellectual property theft, introducing errors and compromising the integrity of parts can have notable and catastrophic effects.

A study by Belikovetsky et al. [27] introduced a stress concentration into one propeller blade of a drone by adding an imperfection into the original CAD file. Since the AM manufacturing workflow is vulnerable to system attacks due to the vulnerability in the software tools and the network connecting the various components [9,10], a defect introduced early on in the CAD modeling stage will penetrate easily deceiving the other steps. The imperfection, while undetectable through visual inspection and standard metrology methods, caused catastrophic failure mid-flight, leading to a crash. While crashing a drone is a fairly harmless demonstration, it shows the danger of introducing errors into parts necessary. Other researchers such as Wu et al. [20] and Sturm et al. [28] used the same void introduction technique to compromise mechanical integrity and showed that visual inspection and standard metrology methods were insufficient in detecting attacks. When AM becomes more widely used in the manufacture of medical devices [29,30], the integrity of the printed pieces must be ensured to maintain patient safety. In aeronautics, printed pieces can be safety-critical components with complex thermal and mechanical properties [31,32]. Introducing errors into the design could result in changes to these properties, ultimately leading to catastrophic failure.

From previous studies [33,34], we have identified variation in speed and temperature to be the critical elements that affect the accuracy of the geometric features [35] in printed pieces. Components whose speed can be varied include the extruder motor, end-effector, and printbed, among others [36]. In this paper, we are interested in studying early-stage defect detection and in particular defects introduced at the CAD model stage. As a result of early-stage compromise, the defects are eventually propagated further into the AM workflow, generating erroneous G codes and M codes which again get translated to end-effector movements.

The inspection of parts produced with AM requires the characterization of external and internal geometry. Non-destructive inspection techniques include computed tomography [37–39], ultrasonic imaging [40,41], and impedance testing [42,43]. While capable of mapping internal geometry with high resolution, each of these methods is expensive and requires time for measurement and analysis. In situ monitoring has been suggested as a method of QA/QC that requires little or no additional time for analysis [44–47].

Companies such as Identify 3D[1] and 3DP Security[2] have emerged to provide IT solutions to ensure the integrity of data in AM systems. Identify 3D provides a suite of software that helps customers ensure the integrity of printed designs,[3] while 3DP Security employs various techniques to protect the intellectual property rights of designers and companies [48]. However, the diversity of possible cyber-attacks requires a solution that is robust and easily adapted to a wide array of machines. Furthermore, cyber-security solutions, can be costly [49,50] of a manufacturing process. Less intrusive solutions that minimize necessary modifications to the manufacturing machine are thus preferred.

2.2 Image Based Motion Analysis for Understanding Structural Change. The discontinuities due to deviation from optimal process flow settings can be attributable to the introduction of defects via system hacks [51]. Structural health monitoring (SHM) techniques focus on extracting the dynamic response of structural systems to assess process condition, detect possible damage detection or residual life prediction of a structure. Videos are well-suited for AM system monitoring because they provide non-contact, real-time, high-dimensional signals as a sequence of snapshots across time. Conventional non-destructive testing techniques may not be well-suited for SHM because they cannot assist in real-time structural monitoring and require laboratory-grade equipment to characterize defects and/or perform condition analysis [52–54]. Therefore, these techniques along with other imaging-based techniques such as micro CT scanning fall under preventive maintenance methodologies. However, predicting a defect/compromise as its progressing is much more beneficial in terms of time, money, and resources along with limited to decreased downtime [55,56]. Hence, the parameters such as the size, price, and a requirement for an optimal sensor network arrangement which is sensitive in picking up varying frequency signals yet robust to noise is essential in order to provide a real-time feedback and monitoring assessments [56]. For this reason, optical monitoring methods are increasingly being studied and are also being used for structural dynamics identification and in SHM systems [57,58].

Image processing techniques do not explicitly capture the displacements of components from a sequence of images. They often approximate the motion field via motion estimation techniques which can often capture motion noise, which then offsets the frequency spectrum of the underlying signal of interest [58,59]. Phase variations corresponding to structural changes in a sequence of images captures the motion-field information and can be temporally processed to reveal imperceptible motions, with robustness to noise [59,60].

[1]https://identify3d.com/
[2]https://identify3d.com/trace/
[3]https://identify3d.com/protect/, https://identify3d.com/manage/, https://identify3d.com/enforce/, https://identify3d.com/trace/

Earlier studies have used phase-based motion magnification to extract the operating deflection shapes of the structures, damage characterization, and modal analysis [59,61–64]. There have been studies proposed in AM that utilize computer vision techniques to detect defects by using automated process monitoring techniques capable of working in real-time and offline [3,4,65,66]. A support vector machine approach to perform automatic defect identification is presented in the paper by Delli and Chang [3], where they classify parts as good or defective based on images samples captured during the printing process. Though machine learning techniques provide an edge over classification accuracies, they are restricted by data wherein a diverse sample involving diverse defects is required to qualify as a generalizable defect classifier. Additionally, the method is limited by camera orientation and requires stopping the printing process temporarily to perform image classification. Gobert et al. [4] proposed using an ensemble classifier to perform a binary classification during the printing process to detect defects with the help of images captured using an in situ DSLR camera with the 3D CT scan data of the layers as ground truth. Though their method allows for layer level defect identification, it is limited in data by the supervised approach and the use of a DSLR camera attached to the printer. Holzmond and Li [65] proposed another in situ method to identify defects and attacks by performing a 3D image correlation of the part being printed with the computer model of the part. This method also relies on the use of an industrial-grade high-cost camera. Rather than adding sensors or industrial grade cameras to existing AM machines, our method uses an off-the-shelf camera with no contact with the printer to perform defect detection using unlabeled image data. Our method compares the temporally encoded motion of a compromised image sequence with that of an uncompromised image sequence to identify variations thereby avoiding the issue of subjectivity of the nature of the defect. Such a feat previously required the use of labeled data and is susceptible to the problem of differentiating between void as a feature and void as a defect. Finally, our method will help generate important lower dimensional spatio-temporal features from a higher dimensional video data of the system under study as opposed to making a classification based on the higher dimensional pixel data.

2.3 Research Hypotheses. Based on the concomitant gaps in the literature, this study seeks to answer two research questions, namely:

RQ-1: Can the magnitude of the amplitude envelope from an image sequence of the AM printing process detect system compromise?

H_{o1}: There is no difference in means between the mean amplitude envelope of a template image sequence and a compromised image sequence.

H_{a1}: There is a difference in the mean amplitude envelopes of a template image sequence and a compromised image sequence.

RQ-2: Can the instantaneous phase response from an image sequence of the AM printing process detect system compromise?

H_{o2}: There is no difference in means between the instantaneous phase response of a template image sequence and a compromised image sequence.

H_{a2}: There is a difference in the mean instantaneous phase response of a template image sequence and a compromised image sequence.

Section 3 will introduce the method of phase-based video amplification in the context of AM and the corresponding algorithmic steps toward feature extraction.

3 Method

The ability to reconstruct an image depends on both (i) *magnitude* (i.e., information on color) and (ii) *phase* (i.e., information on features/edges). The method outlined in Fig. 1 employs the concepts of phase and magnitude for image processing and reconstruction to detect a compromise in a 3D-printing process using captured video data. Given an input of the video recording of a compromised printing process (see Fig. 1), the image sequence in the recording is phase amplified (*Phase amplification of Image Sequence*) as explained in Sec. 3.1. On completion of phase amplification, we transform the image sequence (*Sequence Transformation and Detection*) to an analytic image sequence to identify intentionally induced sample defects in the spatio-temporal domain as explained in Sec. 3.2.

3.1 Phase Amplification of Image Sequence. Let function $f{:}x, y \rightarrow I \in \mathbb{R}^N$ map spatial position of the pixels along the X and Y axes of an image from the input image sequence $V{:}f \in V$ to an intensity profile I, where $x, y \in \mathbb{R}^{NxN}$ represents the $N \times N$ dimensional spatial arrangement of the pixels. Our fundamental assumption is that with no change in global (camera) and local (printer) positions, the motion of the end-effector which is the print head and any moving component on the printer are the only sources of motion which get encoded in the phase of the image from one frame to another in the image sequence V. According to the Fourier transform shift theorem, any change in the spatial domain will lead to a proportional change in phase in the frequency domain of the corresponding image function [67]. This suggests that motion magnification within a selected frequency band corresponding to the natural frequencies of the moving components will preserve their original motion information by preserving the phase variations within the same band. The *fast Fourier transform (FFT)* of the spatio-temporal image sequence decomposes an image as a linear combination of Fourier basis elements as given by Eq. (1).

$$f(x, y) = \sum_{\omega_x=-\infty}^{\infty} \sum_{\omega_y=-\infty}^{\infty} F(\omega_x, \omega_y) e^{i(\omega_x x + \omega_y y)} \tag{1}$$

where, $f(x, y)$ is the original image in which each band corresponds to a single frequency (ω_x, ω_y) in the X and Y axes, respectively, while $(\omega_x x + \omega_y y)$ corresponds to the phase of the complex sinusoid $(F(\omega_x, \omega_y)e^{i(\omega_x x+\omega_y y)})$ and F denotes the amplitude of an image sample in the Fourier domain. The image sequence as depicted in the AM workflow in Fig. 1 represents an entire printing process, wherein the motion of the various moving components (print bed and print head) in the X and Y dimension of the camera frame is captured spatio-temporally. In this paper, we adopt the steerable pyramid approach and the image displacement profile as used in Wadhwa et al. [59]. We present the case of a global translation of a motion (aggregate motion of all moving components in the printer) over time using a displacement profile $((x + \delta(t), y + \delta(t)))$ which is combined with Eq. (1) to represent the displaced Fourier decomposition as given by Eq. (2). Alternatively, it is possible to use a Lagrangian approach [68,69] involving the use of compute-intensive optical flow vectors to represent the motion field. The use of a steerable pyramid is favored due to the properties of the transformation such as non-aliased sub-bands and quadrature-phase filters that avoid spatial aliasing. Additionally, spatial decomposition into spatial bands allow band-specific temporal filtering thereby reducing amplification errors which in turn allows for meaningful phase measurements.

$$f(x + \delta(t), y + \delta(t)) = \sum_{\omega_x=-\infty}^{\infty} \sum_{\omega_y=-\infty}^{\infty} F(\omega_x, \omega_y) e^{i(\omega_x(x+\delta(t))+\omega_y(y+\delta(t)))} \tag{2}$$

where $\omega_x(x + \delta(t)) + \omega_y(y + \delta(t))$ represents the phase shift corresponding to a global translation and $\delta(t)$ is the displacement function which provides the local spatial motion information. For the sake of simplification, let $H_\omega(x, y, t)$ be a complex sinusoid such that $H_\omega(x, y, t) = F(\omega_x, \omega_y)e^{i(\omega_x(x+\delta(t))+\omega_y(y+\delta(t)))}$. Unlike the Laplacian pyramid or the Gabor filter, the directional derivative operators of the steerable pyramid provide a translation and rotation invariant

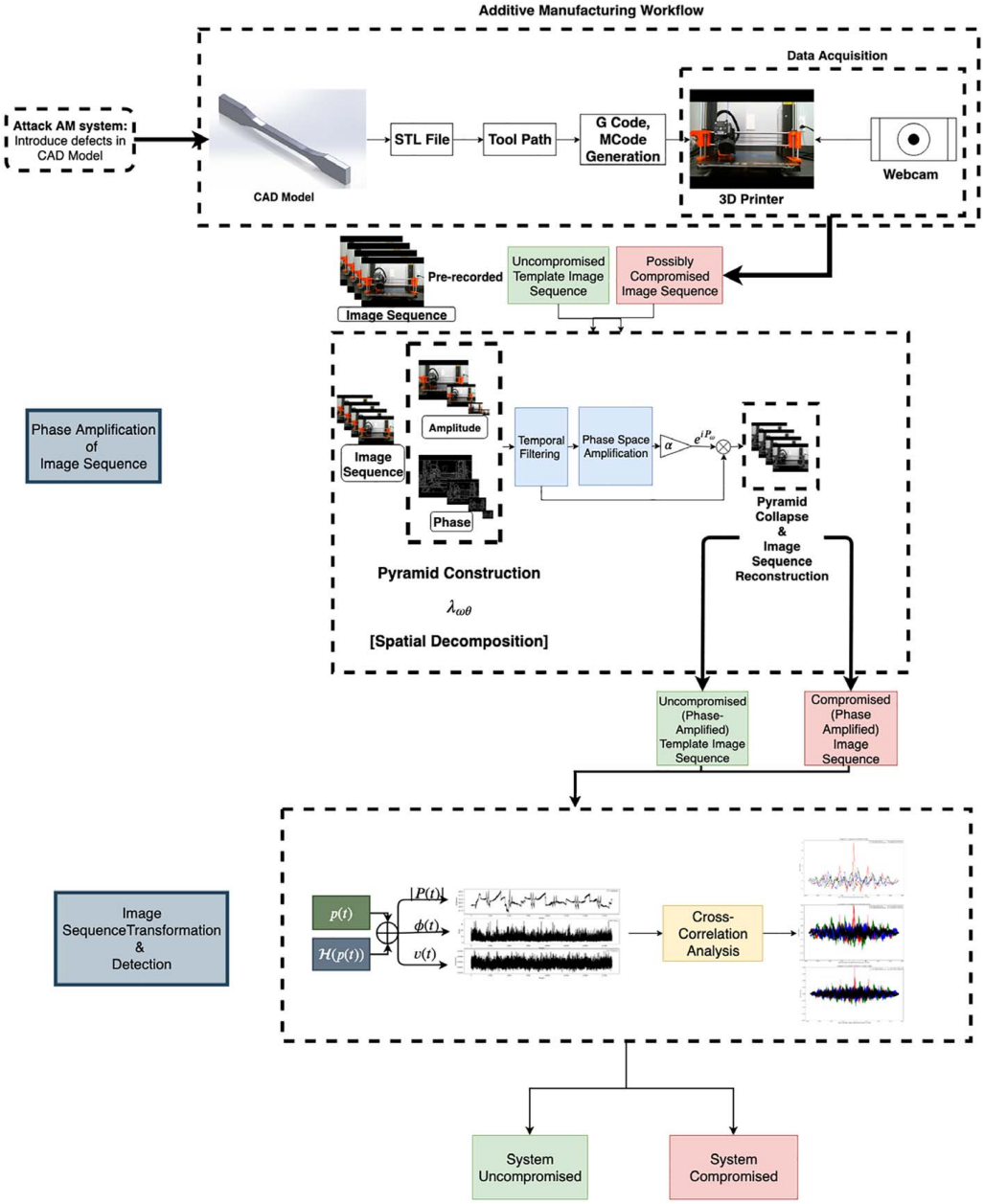

Fig. 1 Process diagram of the proposed video-based method

representation of the image structure. This allows phase variations to become detectable in multiple camera orientations. The motion amplified reconstruction of the image, given a construction of the steerable pyramid ($\lambda_{\omega,\theta}$) is given by Eq. (3), depicting the build and collapse of the steerable pyramid in the frequency domain.

$$f(x+\delta(t), y+\delta(t)) = \sum_{\omega_x=-\infty}^{\infty} \sum_{\omega_y=-\infty}^{\infty} H_\omega(x, y, t)\lambda_{\omega,\theta}^2 \quad (3)$$

Since the FFT computes the magnitude and phase over time at every spatial scale and orientation of the pyramid, we temporally bandpass filter the phase spectrum corresponding to the frequency bands of interest (in our case, the harmonic frequencies of the moving component in the system). The frequency band here refers to the band within which the motion information of the moving component(s) is encoded. The image samples are bandpass filtered in the 0–15 Hz range based on empirical analysis as no frequencies above 15 Hz resulted in significant amplification of the print head motion. The bandpassed phase ($P_\omega(x, y, t) = \omega\delta(t)$) is then multiplied by a suitable amplification factor (α) and convolved with $H_\omega(x, y, t)$ to collapse the pyramid as given by Eq. (4).

$$f(x+(1+\alpha)\delta(t), y+(1+\alpha)\delta(t)) = \sum_{\omega_x=-\infty}^{\infty} \sum_{\omega_y=-\infty}^{\infty} H_\omega e^{i\alpha P_\omega} \lambda_{\omega,\theta}^2 \quad (4)$$

$f(x+(1+\alpha)\delta(t), y+(1+\alpha)\delta(t))$ as given by Eq. (4) is a motion magnified image. This process of forming a steerable pyramid and collapsing to reconstruct a phase amplified image sequence is performed iteratively for each image in the sequence. By phase-amplifying the image sequence, we have amplified all imperceptible movements in the bandpass (continuous simple harmonic oscillations as a result of repetitive translational movements). Since the defects introduced onto the samples are small, the phase-amplification step helps amplify changes representative of missing tool path movements. Section 3.2 will introduce a basis for observing the energy variations as a result of defect formation within the spatio-temporal domain.

3.2 Image Sequence Transformation and Detection. Each image in the sequence of images in V_{temp} and V_{sample} is subject to motion magnification as described in Sec. 3.1 and reconstructed to form the motion magnified video $\hat{V}_{template}$ and $\hat{V}_{sample}$, where $\hat{V}_{template}$ is the image sequence corresponding to the uncompromised printing process while $\hat{V}_{sample}$ is the image sequence of the compromised printing process subject to process monitoring. Since many of the naturally occurring signals exhibit time-varying parameters, it becomes important to analyze the time-varying motion magnified image sequences. The objective of the method is to observe a deviation in the positioning of the moving component(s) over time (spatio-temporal flow), between image sequences. However, given the phase amplified spatio-temporal sequence, the *Uncertainty Principle* causes a time-frequency trade-off, causing the sequence to lose temporal resolution in favor of frequency resolution if analyzed in the frequency domain. To work around the limitation imposed by the *Uncertainty Principle* and to describe a signal simultaneously in time and in frequency, we construct the analytical signal of the spatio-temporal sequence [67]. By localizing the amplitude, phase and frequency distribution of the image sequence, we construct a complex-valued representation of the time-varying function $f(x + (1 + \alpha)\delta(t), y + (1 + \alpha)\delta(t))$ such that the real and the imaginary parts are related to each other via the Hilbert transform. Additionally, since most of the information in the reconstructed image sequence is redundant, important features such as instantaneous amplitude envelope, phase, and frequencies are extracted as properties of the analytical signal to decrease the original dimensionality of the image sequences. An analytical signal is a signal in which negative frequency components can be discarded with no loss in information [67] and is formulated as follows:

$$P(t) = p(t) + j\,\mathcal{H}[p(t)] \tag{5}$$

where $P(t)$ is the analytic signal constructed from $p(t) = f(x + (1 + \alpha)\delta(t), y + (1 + \alpha)\delta(t))$ and $\mathcal{H}$ is a linear Hilbert transform operator. It is clearly evident that the imaginary component of the analytic signal ($P(t)$) is the Hilbert transform of the real-valued signal, and the real signal $p(t)$ can always be retrieved by setting the imaginary component $\mathcal{H}[p(t)] = 0$ to zero. The transformation of the original signal and the extraction of the signal properties is outlined in the *Image Sequence Transformation and Detection* step in Fig. 1. The instantaneous amplitude (envelope extraction) is computed as $|P(t)| = \sqrt{p(t)^2 + \mathcal{H}[p(t)]^2}$, while the instantaneous phase is computed as $\phi(t) = \angle P(t) = \arctan[\mathcal{H}[p(t)]/p(t)]$ and the instantaneous frequency is computed as $v(t) = (1/2\pi)(d/dt)\phi(t)$. Having derived the envelope, the instantaneous phases and frequencies of the analytic signal, we now have a decomposed representation of the spatio-temporal flow corresponding to the AM printing process. We use the mean amplitude envelope and the instantaneous phase responses of the image sequence extending to time t to differentiate between samples to identify system compromise and the type of defect via a cross-correlation analysis, which is described in Sec. 5. Section 4 discusses the experimental protocol and sample data collection while Sec. 5 describes statistical tests and cross-correlation analysis.

4 Experiments and Data Collection

The following sections describe the experimental setups, data format, and storage. We perform an experiment as described in Sec. 4.1 to collect data for analysis using our method. Section 4.2 describes a tensile testing experiment that is conducted to observe the effectiveness of conventional techniques on identifying system compromise.

4.1 Case Study 1: Data Collection for Validating the Video-Based Method. The researchers used a Prusa i3 MK3 to print 10 ASME Type-1 tensile bars. The tensile bars (see Fig. 2) were printed with poly-lactic acid at a thickness of 3.2 mm. The tensile bars were printed with an extruder nozzle temperature of 210 deg and a heated bed temperature of 60 deg. Before image processing analysis, each tensile bar was weighed with a spirit digital scale. The mean and standard deviation of the mass of the 10 tensile bars was calculated to establish a range of acceptable masses.

An intentionally introduced attack was performed on the original CAD model to produce a 0.2 mm by 5.0 mm void near one shoulder of the tensile bar. The placement of the void was based on work in previous literature [28]. The depth of the void varied for three levels of concealment, *tier-1*: full-depth void (thickness of full-thickness void: 3.2 mm), *tier-2*: partial-depth void (thickness of partial-thickness void: 1.6 mm) originating from the surface, and *tier-3*: internal void (thickness of internal void: 2.4 mm). The length of the defect was just over 3% of the total length of the tensile bar. The width of the defect was just over 1% of the total width of the tensile bar. However, due to the placement of the full thickness void, the cross-sectional area at the medial end of the defect was decreased by nearly 15%. The mass of these altered tensile bars was collected to compare with the 10 unaltered tensile bars. As no prior dataset corresponding to non-contact, non-invasive structural defect detection exists, we created one containing video sequences with each video recording lasting the entire print duration of 30 min of 10 no void base samples, as well as 6 samples with included voids: 2 *tier-1*, 2 *tier-2*, and 2 *tier-3*. The image samples are amplified by a factor (α) equals 40 and bandpass filtered in the $0 - 15$ Hz range based on empirical analysis as no frequencies above 15 Hz resulted in significant amplification of the print head motion. The experimental setup is illustrated in Fig. 3. This setup ensures that the camera is positioned parallel to the 3D printer

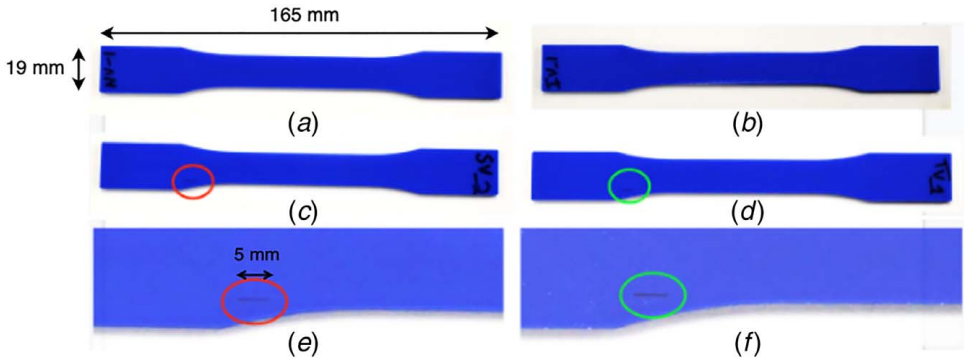

Fig. 2 Analyzed samples (circled spots indicate voids): (*a*) tensile bar with no void, (*b*) tensile bar with internal void, (*c*) tensile bar with single side void, (*d*) tensile bar with through void, (*e*) enlarged view of tensile bar with single side void, and (*f*) enlarged view of tensile bar with through void

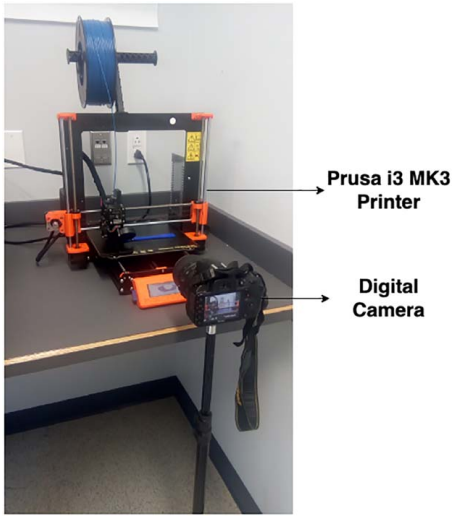

Fig. 3 Experimental setup

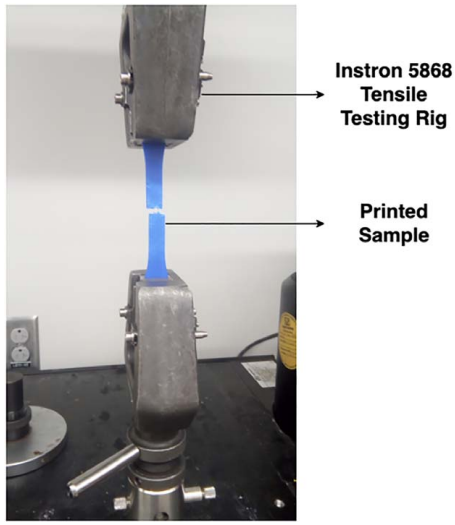

Fig. 4 Printed sample subject to tensile testing

such that there is no physical contact between the printer and the camera, thereby isolating the vibration of the 3D printer from affecting the data collection. Videos are recorded in a 24-bit *RGB* color format at 29.97 frames/second (NTSC video standard) and a resolution of 1920×1080 and stored in H.264/advanced video coding (AVC) format. However, for the study and analysis, we downsampled the resolution of the video to 640×480. Our fixed factor was the sample design while our variables included the tiers of defects with the response measured being the phase-plane variations.

4.2 Case Study 2: Tensile Testing on Printed Samples. We are interested in comparing the effectiveness of conventional mechanical tests to that of our method. Tensile testing is a fundamental technique used in the mechanical and material sciences to determine the properties of a material. By subjecting the printed samples to tensile testing, we expect to understand the effectiveness of the test in detecting defects post-printing to identify possible system compromise. We follow a protocol similar to that of Zeltman et al. [48] and according to ASME standards [70], which is conducted to observe the effectiveness of conventional techniques on identifying system compromise. The tensile testing was performed on an Instron 5868 tensile testing rig with a 10 kN load cell. All specimens (refer Sec. 4.1) were pulled at a rate of 10 mm/min. Stress was calculated using a cross-sectional area of 41.6 mm^2, from a width of 13 mm and a thickness of 3.2 mm. Strain was calculated using a gauge length of 50 mm. The experimental setup of the apparatus and the specimen (after testing) is as shown in Fig. 4. The stress-strain curves were plotted while ultimate tensile strength, elongation at fracture, and modulus of elasticity were calculated for further analysis.

Section 5 elucidates the application of the algorithm, the corresponding statistical analysis on the effectiveness of our method and that of the tensile test.

5 Results and Discussion

Prior to analyzing the printed samples using the video-based method and tensile testing, a visual inspection and mass comparison are performed. The mean mass of the 10 unaltered tensile bars was 9.88 g, with a standard deviation of 0.06 g. Each of the tensile bars with an internal void fell within 1 standard deviation of the mean, while the tensile bars with a full-depth void and partial-depth void fell within 2 standard deviations. This suggests that tensile bars with internal voids cannot be differentiated from unaffected tensile bars through either mass or visual inspection and that other detection methods must be employed. To that end, the following sections discuss and validate our hypothesis on using the video-based method for detecting system compromise. Additionally, we also subject the printed samples to tensile testing to detect the hacks and we compare the effectiveness with that of the video-based method to show that automated methods are required in the AM cyber-security space.

5.1 Discussion of Case Study 1. For the first case study, we perform offline phase amplification on the video sequences as recorded by the camera as shown in Fig. 3. The amplitude envelope and instantaneous phase variation responses over time are computed to predict a difference in the spatio-temporal flow of $\hat{V}_{template}$ and $\hat{V}_{compromised}$ with a cross-correlation analysis to detect voids caused by system manipulations. We test our hypotheses using responses from the experiment described in Sec. 4.1 to address our research questions. A one-way ANOVA with post-hoc analysis is performed to statistically validate the feasibility of using the video-based method in AM cyber-security. We perform a one-way ANOVA test with four levels in a between groups layout. The levels being compared are (1) no void amplitude envelope/instantaneous phase responses, (2) single side void amplitude envelope/instantaneous phase responses, (3) internal void amplitude envelope/instantaneous phase responses, and (4) through void amplitude envelope/instantaneous phase responses.

Figure 5 depicts the interval plot for each of the levels according to their corresponding descriptive statistical information. There is a

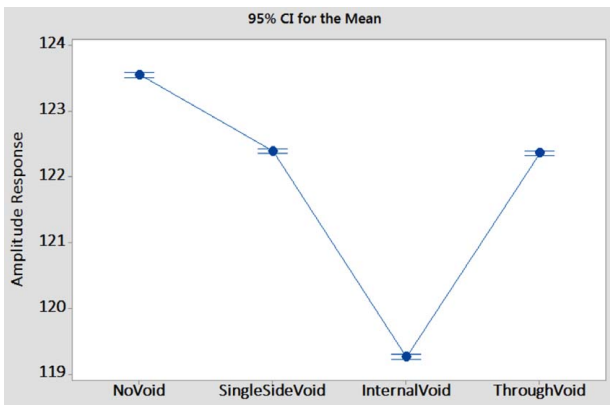

Fig. 5 Interval plot (amplitude responses versus image sequences)

Table 1 Tukey simultaneous tests for differences of means between void levels for amplitude responses

Difference of levels	Difference of means	SE of difference	95% CI	*T*-value	Adjusted *P*-value
Single side void–no void	−1.16	0.026	(−1.23, −1.09)	−45.01	0.000
Internal void–no void	−4.29	0.026	(−4.35, −4.22)	−166.27	0.000
Through void–no void	−1.19	0.026	(−1.26, −1.13)	−46.19	0.000
Internal void–single side void	−3.12	0.026	(−3.19, −3.06)	−121.26	0.000
Through void–single side void	−0.03	0.026	(−0.10, 0.036)	−1.17	0.645
Through void–internal void	3.10	0.026	(3.03, 3.16)	120.08	0.000

clear difference between the means of no-void, single side void, internal void, and through void amplitude responses as observable in Fig. 5, which in turn presents a case for rejecting the null hypothesis (H_{o1}) with *P*-value <0.05. However, a one-way ANOVA only identifies if there exists a difference in mean amplitude envelope responses between the groups without specifying the groups whose mean vary in comparison to that of No Void responses. Thus, we perform the Tukey's simultaneous tests for differences of means between the levels being compared, whose analysis is described in Table 1. If the C.I. does not possess "0" in its interval, then the comparing sequences have a significant difference in means. However, the Tukey's test reveals an interesting result, there is no difference in means between single void and through void responses. The physical difference between the single void and through void sample is attributable to the additional layer of thickness found in the single void sample. This result suggests a possible limitation in using amplitude envelope responses to detect defect or compromise at the layer level if the differences between samples are minute or are not significant as in the case of no void–internal void comparison.The results of the second hypothesis test are illustrated using an interval plot comparison as shown in Fig. 6, while Table 2 describes the Tukey's test statistics. Like the concluded hypothesis test, this test also finds a significant mean difference between the comparing levels with *P*-value <0.05. The instantaneous phase response is able to observe the difference in layer thickness between a single void and through void sample with a higher significance in difference of mean. This statement is corroborated by Table 2, while Fig. 6 depicts the 95% CI (confidence interval) for the means of each pair of comparing levels. This differentiability of the method in observing layer level thickness change between two samples (single void sample and through void sample) is a result of motion encoding via instantaneous phase responses, which varies in the same time period as a result of the addition of material in the single void sample. However, though the Tukey's test metrics were within the significance threshold for each of the sample pairs, no void and through void samples share an overlapping phase distribution. This suggests verifying two probable hypotheses: (i) The size of the void is not large enough to be detected, suggesting that the method is approaching its void difference detectability threshold which requires further sensitivity analysis involving a change in the size of the through void. (ii) Alternatively, the method's signal resolution in capturing changes involving small voids as such (see Fig. 2) could suggest the approaching convergence of the Through Void signal with the No Void signal, in which case a sensitivity analysis involving larger samples with smaller voids could be performed. However, since this is a study showing the feasibility of the method in detecting system compromises using an image processing algorithm, we devote the analysis to a future study with a larger sample size.

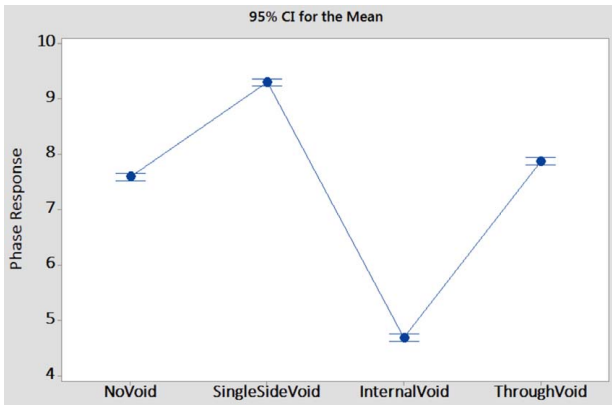

Fig. 6 Interval plot (instantaneous phase responses versus image sequences)

At the outset, the instantaneous phase responses coupled with the magnitude responses are able to differentiate between the defect types, thereby complementing their ability in detecting system compromise.

Though the initial objective of the paper is to observe changes in spatio-temporal flow correlative of intentionally introduced defects, the use of amplitude envelope and instantaneous phase responses presents a promising case of differentiating between samples with varying defect patterns. Since characterizing AM part defects is not within the scope of this paper, we present a cross-correlation analysis which not only detects a system compromise, but also the variations in system compromise with varying system manipulation. Cross-correlation takes as its input two comparing functions and slides one along the *x*-axis of the other to understand if they are identical. By sliding along each discrete point in the *x*-axis, the integral of their dot product at each position is calculated, thus completing the cross-correlation analysis. We compute the cross-correlation between the amplitude envelope magnitude and instantaneous phase of $\hat{V}_{NoVoid}$ and each of the remaining image sequences ($\hat{V}_{SingleSideVoid}$, $\hat{V}_{InternalVoid}$, $\hat{V}_{ThroughVoid}$) as given by the following equations:

$$[|P_i|*|P_{NoVoid}|](\tau) = \sum_{t=-N_{\max}}^{N_{\max}} |P_i|(t-\tau)|P_{NoVoid}|(t) \tag{6}$$

Table 2 Tukey simultaneous tests for differences of means between void levels for instantaneous phase responses

Difference of levels	Difference of means	SE of difference	95% CI	*T*-value	Adjusted *P*-value
Single side void–no void	1.71	0.048	(1.58, 1.83)	35.49	0.000
Internal void–no void	−2.91	0.048	(−3.03, −2.79)	−60.50	0.000
Through void–no void	0.28	0.048	(0.15, 0.40)	5.75	0.000
Internal void–single side void	−4.62	0.048	(−4.74, −4.49)	−95.99	0.000
Through void–single side void	−1.43	0.048	(−1.55, −1.31)	−29.74	0.000
Through void–internal void	3.12	0.048	(3.06, 3.31)	66.25	0.000

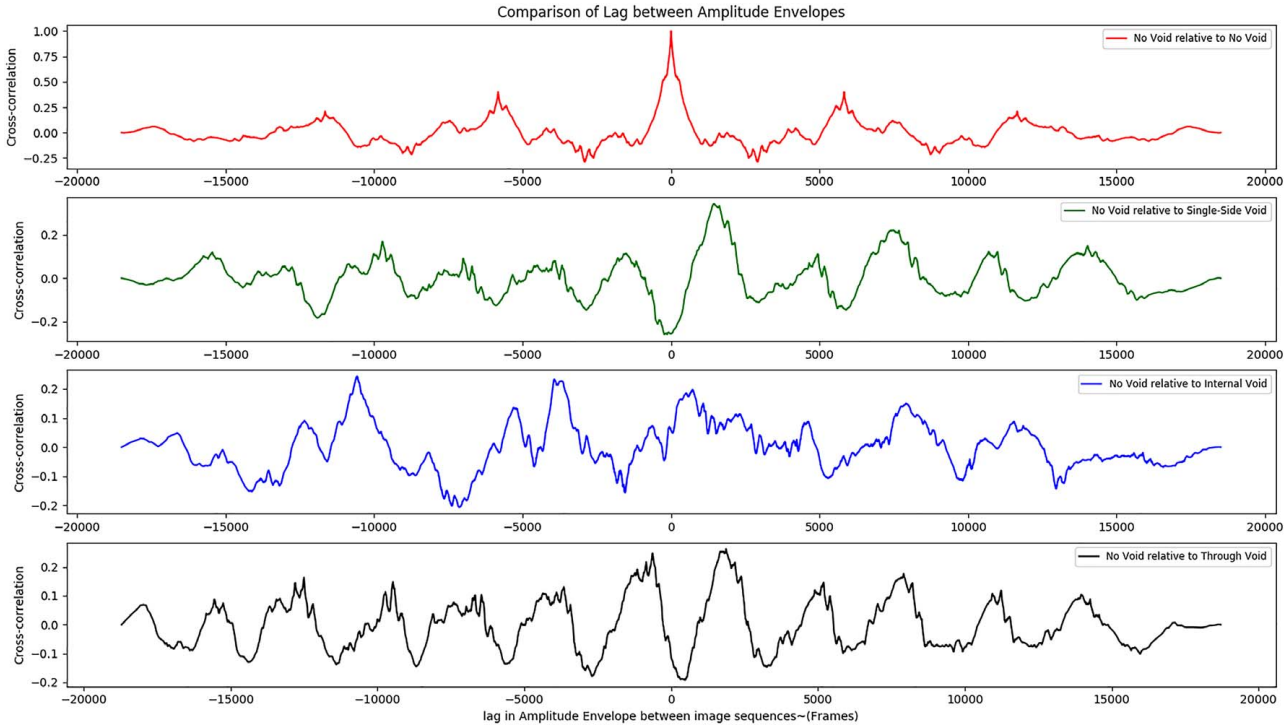

Fig. 7 Cross-correlation between the amplitude envelopes

$$[\phi_i * \phi_{NoVoid}](\tau) = \sum_{t=-N_{\max}}^{N_{\max}} \phi_i(t-\tau)\phi_{NoVoid}(t) \tag{7}$$

where $i \in \{Single\ Side\ Void, Internal\ Void, Through\ Void\}$ and τ is the time point called time-lag wherein the cross-correlation between the image sequences is calculated. In Eqs. (6) and (7), $N_{\max} = \max\{N_{NoVoid}, N_i\}$ where N is the number of samples/frames in the image sequence and the time-lag $\tau = 0, \pm 1, \pm 2, \ldots, \pm N_{\max}$.

The results of the cross-correlation analysis are illustrated in Fig. 7 for comparing cross-correlations of the magnitude of amplitude envelope and Fig. 8 for comparing cross-correlations of instantaneous phase responses. The comparison of cross-correlations between $\hat{V}_{NoVoid}$ and each of $\hat{V}_{SingleSideVoid}$, $\hat{V}_{InternalVoid}$, $\hat{V}_{ThroughVoid}$ as provided by Fig. 7 indicates the following: (1) The image sequences $\hat{V}_{SingleSideVoid}$, $\hat{V}_{InternalVoid}$, $\hat{V}_{ThroughVoid}$ are correlative of a possible system compromise via induced defects as none of the cross-correlations agree with the auto-correlation of $\hat{V}_{NoVoid}$.

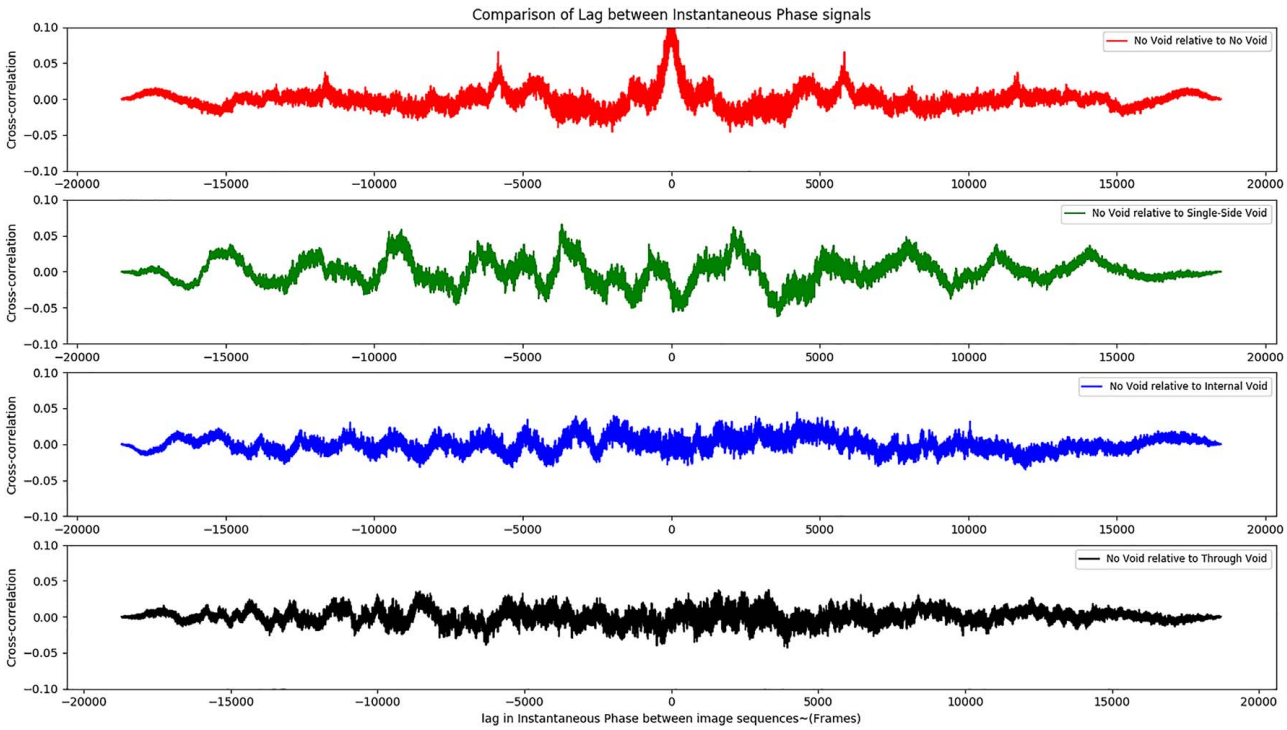

Fig. 8 Cross-correlation between the instantaneous phase responses

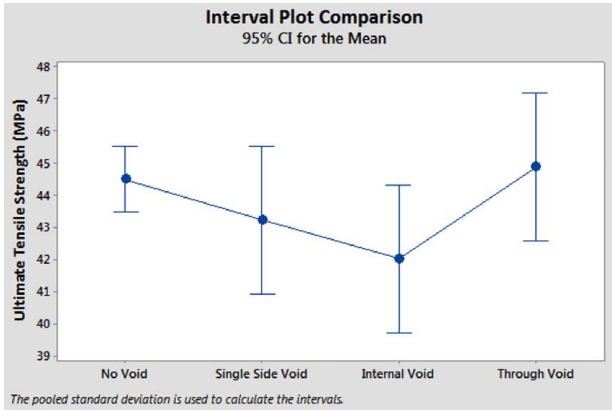

Fig. 9 Interval plot (ultimate strength responses versus image sequences)

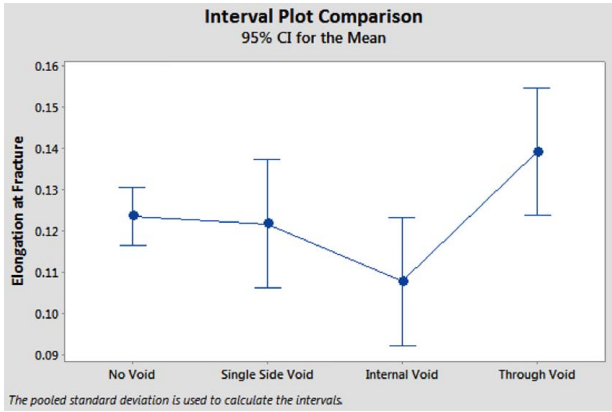

Fig. 10 Interval plot (elongation at fracture responses versus image sequences)

(2) Cross-correlation between $\hat{V}_{NoVoid}$, $\hat{V}_{SingleSideVoid}\hat{V}_{NoVoid}$, $\hat{V}_{SingleSideVoid}$ and $\hat{V}_{NoVoid}$, $\hat{V}_{ThroughVoid}\hat{V}_{NoVoid}$, $\hat{V}_{ThroughVoid}$ (black line) suggest that they have an agreeing cross-correlation as revealed by their aligning cycles due to a difference in layer thickness only, thus agreeing with our Tukey's test of difference in finding a similarity in signal response distribution.

Consequently, the comparison of cross-correlations between $\hat{V}_{NoVoid}$ and each of $\hat{V}_{SingleSideVoid}$, $\hat{V}_{InternalVoid}$, $\hat{V}_{ThroughVoid}$ as provided by Fig. 8 indicates the following: (1) The image sequences $\hat{V}_{SingleSideVoid}$, $\hat{V}_{InternalVoid}$, $\hat{V}_{ThroughVoid}$ are correlative of a possible system compromise via induced defects as none of the cross-correlations agree with the auto-correlation of $\hat{V}_{NoVoid}$. (2) There is compelling visual evidence suggesting alternating phase variation between the $\hat{V}_{SingleSideVoid}$, $\hat{V}_{InternalVoid}$, and $\hat{V}_{ThroughVoid}$ samples.

5.2 Discussion of Case Study 2. We perform tensile testing on the printed samples as described in Sec. 4.2. Based on the characteristics of the samples, the test computes the ultimate strength and elongation at fracture responses. Though we have shown that the video-based method can be used in detecting system compromise, we are interested to know if a standard test such as tensile test can be performed on printed samples to identify defects and hence system compromise. However, our study has an unbalanced sample size (the number of No Void prints are higher in number). Though ANOVA is robust to violations of the normality assumption, departure from the assumption of homoscedasticity increases Type-1 errors. Prior to performing ANOVA, we perform Levene's test to check that the assumption of homogeneity of variance holds. With a *P*-value of 0.469, we fail to reject the null hypothesis (all variances are equal) when the responses are ultimate strength. With a *P*-value of 0.921, we fail to reject the null hypothesis when the responses are elongation at fracture. Additionally, the linearity of the points when a normal probability plot was generated suggests that the data are normally distributed for both the responses. Thus, the assumptions for ANOVA were not violated and a one-way ANOVA with post-hoc analysis was performed between the four void types with the responses being the ultimate strength and elongation at fracture. Figure 9 illustrates the 95% confidence interval comparing the void types against the ultimate tensile strength. The test fails to reject the null hypothesis (all means are equal) with a *P*-value of 0.178 (significance level 0.05). Further, Tukey's test results as tabulated in Table 3 fails to find between group significance thereby highlighting that the differences in ultimate tensile strength cannot be used as a measure to identify system compromise. Figure 10 illustrates the 95% confidence interval comparing the void types against the elongation at fracture responses. The test fails to marginally reject the null hypothesis (all means are equal) with a *P*-value of 0.059 (significance level 0.05) suggesting a possible between group significance. Tukey's test results as tabulated in Table 4 finds a statistical significance between through void and internal void samples only. Though the differences in elongation at fracture between void types were significant for one of the pairs, the effectiveness of tensile testing as a viable technique in distinguishing between sample types is inconsistent.

Given that no statistically significant differences could be observed or measured in the mechanical testing between void parts and no void parts, we conclude the discussion by stating that traditional quality checks (mass comparison, visual inspection, and failure testing) are insufficient to identify the voids. However, the video magnification-based method introduced in this work was able to identify the defects.

6 Conclusion and Future Work

Given the need for cyber-security measures in cyber-physical systems associated with additive manufacturing, the paper presents a method for analyzing the spatio-temporal flow of a phase-magnified image sequence of a 3D-printing process captured using an off-the-shelf camera. Specifically, this work exploits the Eulerian approach of observing a defined window and tracking the changes in the phase of an image sequence, while amplifying the changes and performing sequence reconstruction. In this way, motion information over time is embedded into a recorded image

Table 3 Tukey simultaneous tests for differences of means between void levels for ultimate strength responses

Difference of levels	Difference of means	SE of difference	95% CI	*T*-value	Adjusted *P*-value
Single side void–no void	−1.27	1.16	(−4.73, 2.18)	−1.10	0.699
Internal void–no void	−2.49	1.16	(−5.94, 0.96)	−2.14	0.196
Through void–no void	0.38	1.16	(−3.07, 3.83)	0.33	0.987
Internal void–single side void	−1.21	1.50	(−5.67, 3.24)	−0.81	0.849
Through void–single side void	1.65	1.50	(−2.80, 6.11)	1.10	0.695
Through void–internal void	2.87	1.50	(−1.59, 7.33)	1.91	0.274

Table 4 Tukey simultaneous tests for differences of means between void levels for elongation at fracture responses

Difference of levels	Difference of means	SE of difference	95% CI	*T*-value	Adjusted *P*-value
Single side void–no void	−0.00179	0.0078	(−0.0249, 0.0213)	−0.23	0.995
Internal void–no void	−0.01579	0.0078	(−0.0389, 0.0073)	−2.03	0.231
Through void–no void	0.01562	0.0078	(−0.0075, 0.0387)	2.01	0.239
Internal void–single side void	−0.0140	0.010	(−0.0439, 0.0158)	−1.39	0.526
Through void–single side void	0.0174	0.010	(−0.0124, 0.0473)	1.73	0.350
Through void–internal void	0.0314	0.010	(0.0016, 0.0613)	3.12	0.038

sequence of a compromised additive manufacturing system. The analytical form of the phase amplified and time variable image sequence (uncompromised and compromised) was then analyzed using the amplitude envelope and instantaneous phase changes over time to identify a compromise. To verify the feasibility of using the amplitude envelope and instantaneous phase of the analytical version of the image sequence, we conduct a case study to analyze the printed samples using our method and describe the feasibility with statistical evidence. The ANOVA results further exemplify the nature of information encoded as magnitude and phase within the image sequence. Furthermore, we subject the samples to mechanical testing to study the effectiveness of the standard tensile testing technique to observe system compromise to show that conventional techniques may not be suitable for addressing the problem under study. The statistical evidence clearly reveals that new methods are required to address the cyber-security problems in the additive manufacturing domain. Though the focus of this paper is on analyzing the effectiveness of using the motion magnification algorithm to perform early stage defect detection in the AM workflow, defects introduced through variation in speed and temperature of components should also be tested to determine the generalizability of the image processing algorithm. This would help determine the usability of the approach for batch process monitoring and increase the potential use cases.

Acknowledgment

This research was funded in part by the Air Force Office of Scientific Research (AFOSR) grant FA9550-18-1-0108. Any opinions, findings, or conclusions found in this paper are those of the authors and do not necessarily reflect the views of the sponsors.

References

[1] Langner, R., 2011, "Stuxnet: Dissecting a Cyberwarfare Weapon," IEEE Secur. Priv., **9**(3), pp. 49–51.
[2] Owolabi, G. M., Swamidas, A. S. J., and Seshadri, R., 2003, "Crack Detection in Beams Using Changes in Frequencies and Amplitudes of Frequency Response Functions," J. Sound. Vib., **265**(1), pp. 1–22.
[3] Delli, U., and Chang, S., 2018, "Automated Process Monitoring in 3D Printing Using Supervised Machine Learning," Proc. Manuf., **26**, pp. 865–870.
[4] Gobert, C., Reutzel, E. W., Petrich, J., Nassar, A. R., and Phoha, S., 2018, "Application of Supervised Machine Learning for Defect Detection During Metallic Powder Bed Fusion Additive Manufacturing Using High Resolution Imaging," Addit. Manuf., **21**, pp. 517–528.
[5] Wu, H.-Y., Rubinstein, M., Shih, E., Guttag, J., Durand, F., and Freeman, W., 2012, "Eulerian Video Magnification for Revealing Subtle Changes in the World," ACM Trans. Graph., **31**(4), pp. 1–8.
[6] Prakash, S. K. A., and Tucker, C. S., 2018, "Bounded Kalman Filter Method for Motion-Robust, Non-Contact Heart Rate Estimation," Biomed. Opt. Express, **9**(2), pp. 873–897.
[7] Benetazzo, F., Freddi, A., Monteriù, A., and Longhi, S., 2014, "Respiratory Rate Detection Algorithm Based on RGB-D Camera: Theoretical Background and Experimental Results," Healthc. Technol. Lett., **1**(3), pp. 81–86.
[8] Wu, D., Terpenny, J., and Schaefer, D., 2017, "Digital Design and Manufacturing on the Cloud: A Review of Software and Services," AI EDAM, **31**(1), pp. 104–118.
[9] Turner, H., White, J., Camelio, J. A., Williams, C., Amos, B., and Parker, R., 2015, "Bad Parts: Are Our Manufacturing Systems at Risk of Silent Cyberattacks?" IEEE Secur. Priv., **13**(3), pp. 40–47.
[10] Moore, S., Armstrong, P., McDonald, T., and Yampolskiy, M., 2016, "Vulnerability Analysis of Desktop 3D Printer Software," 2016 Resilience Week (RWS), IEEE, pp. 46–51.
[11] Liu, X. F., Shahriar, M. R., Al Sunny, S. M. N., Leu, M. C., Cheng, M., and Hu, L., 2016, "Design and Implementation of Cyber-Physical Manufacturing Cloud using MTConnect," ASME 2016 International Design Engineering Technical Conferences and Computers and Information in Engineering Conference, pp. V01BT02A019.
[12] Armstrong, A. P., Barclift, M., and Simpson, T. W., 2017, "Development of CAD-Integrated Cost Estimator to Support Design for Additive Manufacturing," ASME 2017 International Design Engineering Technical Conferences and Computers and Information in Engineering Conference, pp. V001T02A034.
[13] Tupa, J., Simota, J., and Steiner, F., 2017, "Aspects of Risk Management Implementation for Industry 4.0," Procedia Manuf., **11**, pp. 1223–1230.
[14] Peterson, D., 2013, "Offensive Cyber Weapons: Construction, Development, and Employment," J. Strateg. Stud., **36**(1), pp. 120–124.
[15] Weller, C., Kleer, R., and Piller, F. T., 2015, "Economic Implications of 3D Printing: Market Structure Models in Light of Additive Manufacturing Revisited," Int. J. Prod. Econ., **164**, pp. 43–56.
[16] Do, Q., Martini, B., and Choo, K.-K. R., 2016, "A Data Exfiltration and Remote Exploitation Attack on Consumer 3D Printers," IEEE Trans. Inf. Forensics Secur., **11**(10), pp. 2174–2186.
[17] Faruque, A., Abdullah, M., Chhetri, S. R., Canedo, A., and Wan, J., 2016, "Acoustic Side-Channel Attacks on Additive Manufacturing Systems," Proceedings of the 7th International Conference on Cyber-Physical Systems, IEEE Press, p. 19.
[18] Song, C., Lin, F., Ba, Z., Ren, K., Zhou, C., and Xu, W., 2016, "My Smartphone Knows What you Print: Exploring Smartphone-Based Side-Channel Attacks Against 3d Printers," Proceedings of the 2016 ACM SIGSAC Conference on Computer and Communications Security, ACM, pp. 895–907.
[19] Farwell, J. P., and Rohozinski, R., 2011, "Stuxnet and the Future of Cyber War," Survival, **53**(1), pp. 23–40.
[20] Wu, M., Song, Z., and Moon, Y. B., 2017, "Detecting Cyber-Physical Attacks in CyberManufacturing Systems With Machine Learning Methods," J. Intell. Manuf., **30**(3), pp. 1111–1123.
[21] Chen, F., Mac, G., and Gupta, N., 2017, "Security Features Embedded in Computer Aided Design (CAD) Solid Models for Additive Manufacturing," Mater. Design, **128**, pp. 182–194.
[22] Gupta, N., Chen, F., Tsoutsos, N. G., and Maniatakos, M., 2017, "ObfusCADe: Obfuscating Additive Manufacturing Cad Models Against Counterfeiting," Proceedings of the 54th Annual Design Automation Conference 2017, ACM, p. 82.
[23] Fadhel, N. F., Crowder, R. M., and Wills, G. B., 2013, "Approaches to Maintaining Provenance Throughout the Additive Manufacturing Process," World Congress on Internet Security (WorldCIS-2013), IEEE, pp. 82–87.
[24] Chhetri, S. R., Canedo, A., and Faruque, M. A. A., 2018, "Confidentiality Breach Through Acoustic Side-Channel in Cyber-Physical Additive Manufacturing Systems," ACM Trans. Cyber-Phys. Syst., **2**(1), p. 3.
[25] Chhetri, S. R., Faezi, S., Canedo, A., and Al Faruque, M. A., 2016, "Poster Abstract: Thermal Side-Channel Forensics in Additive Manufacturing Systems," Proceedings of the 7th International Conference on Cyber-Physical Systems, Vienna, Austria, Apr. 11–14.
[26] Chhetri, S. R., Canedo, A., and Faruque, M. A. A., 2016, "Kcad: Kinetic Cyber-Attack Detection Method for Cyber-Physical Additive Manufacturing Systems," Proceedings of the 35th International Conference on Computer-Aided Design, Austin, TX, Nov. 7–10, ACM, p. 74.
[27] Belikovetsky, S., Yampolskiy, M., Toh, J., Gatlin, J., and Elovici, Y., 2017, "dr0wned–Cyber-Physical Attack with Additive Manufacturing," 11th {USENIX} Workshop on Offensive Technologies ({WOOT} 17), Vancouver, BC, Canada, Aug. 14–15.
[28] Sturm, L. D., Williams, C. B., Camelio, J. A., White, J., and Parker, R., 2017, "Cyber-Physical Vulnerabilities in Additive Manufacturing Systems: A Case Study Attack on the .STL File With Human Subjects," J. Manuf. Syst., **44**, pp. 154–164.
[29] Rengier, F., Mehndiratta, A., Von Tengg-Kobligk, H., Zechmann, C. M., Unterhinninghofen, R., Kauczor, H.-U., and Giesel, F. L., 2010, "3D Printing Based on Imaging Data: Review of Medical Applications," Int. J. Comput. Assist. Radiol. Surg., **5**(4), pp. 335–341.
[30] Phan, K., Sgro, A., Maharaj, M. M., D'Urso, P., and Mobbs, R. J., 2016, "Application of a 3D Custom Printed Patient Specific Spinal Implant for C1/2 Arthrodesis," J. Spine Surg., **2**(4), p. 314.
[31] Joshi, S. C., and Sheikh, A. A., 2015, "3D Printing in Aerospace and Its Long-Term Sustainability," Virtual Phys. Prototy., **10**(4), pp. 175–185.
[32] Schmelzle, J., Kline, E. V., Dickman, C. J., Reutzel, E. W., Jones, G., and Simpson, T. W., 2015, "(Re) Designing for Part Consolidation: Understanding

the Challenges of Metal Additive Manufacturing," ASME J. Mech. Des., **137**(11), p. 111404.
[33] Günaydın, K., and Türkmen, H. S., 2018, "Common FDM 3D Printing Defects".
[34] Carneiro, O. S., Silva, A. F., and Gomes, R., 2015, "Fused Deposition Modeling With Polypropylene," Mater. Design, **83**, pp. 768–776.
[35] Polak, R., Sedláček, F., and Raz, K., 2017, "Determination of FDM Printer Settings With Regard to Geometrical Accuracy," Proceedings of the 28th DAAAM International Symposium, pp. 561–566.
[36] Baumann, F., and Roller, D., 2016, "Vision Based Error Detection for 3D Printing Processes," MATEC Web of Conferences, Vol. 59, EDP Sciences, p. 6003.
[37] Bibb, R., Thompson, D., and Winder, J., 2011, "Computed Tomography Characterisation of Additive Manufacturing Materials," Med. Eng. Phys., **33**(5), pp. 590–596.
[38] Thompson, A., Maskery, I., and Leach, R. K., 2016, "X-Ray Computed Tomography for Additive Manufacturing: A Review," Meas. Sci. Technol., **27**(7), p. 72001.
[39] du Plessis, A., le Roux, S. G., Booysen, G., and Els, J., 2016, "Quality Control of a Laser Additive Manufactured Medical Implant by X-Ray Tomography," 3D Print. Addit. Manuf., **3**(3), pp. 175–182.
[40] Everton, S., Dickens, P., Tuck, C., and Dutton, B., 2015, "Evaluation of Laser Ultrasonic Testing for Inspection of Metal Additive Manufacturing," Laser 3D Manufacturing Ii, Vol. 9353, International Society for Optics and Photonics, p. 935316.
[41] Lopez, A., Bacelar, R., Pires, I., Santos, T. G., Sousa, J. P., and Quintino, L., 2018, "Non-Destructive Testing Application of Radiography and Ultrasound for Wire and Arc Additive Manufacturing," Addit. Manuf., **21**, pp. 298–306.
[42] Albakri, M., Sturm, L., Williams, C. B., and Tarazaga, P., 2015, "Non-Destructive Evaluation of Additively Manufactured Parts via Impedance-Based Monitoring," Solid Freeform Fabrication Symposium, Austin, TX, Aug. 10–12, pp. 1475–1490.
[43] Tenney, C., Albakri, M. I., Kubalak, J., Sturm, L. D., Williams, C. B., and Tarazaga, P. A., 2017, "Internal Porosity Detection in Additively Manufactured Parts via Electromechanical Impedance Measurements," ASME 2017 Conference on Smart Materials, Adaptive Structures and Intelligent Systems, Snowbird, UT, Sept. 18–20.
[44] Rao, P. K., Liu, J. P., Roberson, D., Kong, Z. J., and Williams, C., 2015, "Online Real-Time Quality Monitoring in Additive Manufacturing Processes Using Heterogeneous Sensors," ASME J. Manuf. Sci. Eng., **137**(6), p. 061007.
[45] Wu, H., Wang, Y., and Yu, Z., 2016, "In Situ Monitoring of FDM Machine Condition Via Acoustic Emission," Int. J. Adv. Manuf. Technol., **84**(5–8), pp. 1483–1495.
[46] Everton, S. K., Hirsch, M., Stravroulakis, P., Leach, R. K., and Clare, A. T., 2016, "Review of In-situ Process Monitoring and In-Situ Metrology for Metal Additive Manufacturing," Mater. Design, **95**, pp. 431–445.
[47] Grasso, M., and Colosimo, B. M., 2017, "Process Defects and in Situ Monitoring Methods in Metal Powder Bed Fusion: A Review," Meas. Sci. Technol., **28**(4), p. 44005.
[48] Zeltmann, S. E., Gupta, N., Tsoutsos, N. G., Maniatakos, M., Rajendran, J., and Karri, R., 2016, "Manufacturing and Security Challenges in 3D Printing," JOM, **68**(7), pp. 1872–1881.
[49] Rowe, B. R., and Gallaher, M. P., 2006, "Private Sector Cyber Security Investment Strategies: An Empirical Analysis," The Fifth Workshop on the Economics of Information Security (WEIS06).
[50] Fielder, A., Panaousis, E., Malacaria, P., Hankin, C., and Smeraldi, F., 2016, "Decision Support Approaches for Cyber Security Investment," Decis. Support Syst., **86**, pp. 13–23.
[51] Wu, D., Ren, A., Zhang, W., Fan, F., Liu, P., Fu, X., and Terpenny, J., 2018, "Cybersecurity for Digital Manufacturing," J. Manuf. Syst., **48**(Part C), pp. 3–12.
[52] Kudva, J. N., Marantidis, C., Gentry, J. D., and Blazic, E., 1993, "Smart Structures Concepts for Aircraft Structural Health Monitoring," Smart Structures and Materials 1993: Smart Structures and Intelligent Systems, Vol. 1917, International Society for Optics and Photonics, pp. 964–971.
[53] Van Way, C. B., Kudva, J. N., Schoess, J. N., Zeigler, M. L., and Alper, J. M., 1995, "Aircraft Structural Health Monitoring System Development: Overview of the Air Force/Navy Smart Metallic Structures Program," Smart Structures and Materials 1995: Smart Structures and Integrated Systems, Vol. 2443, International Society for Optics and Photonics, pp. 277–285.
[54] Lin, X., and Yuan, F. G., 2001, "Damage Detection of a Plate Using Migration Technique," J. Intell. Mater. Syst. Struct., **12**(7), pp. 469–482.
[55] Gupta, A., and Lawsirirat, C., 2006, "Strategically Optimum Maintenance of Monitoring-Enabled Multi-Component Systems Using Continuous-Time Jump Deterioration Models," J. Qual. Maintenance Eng., **12**(3), pp. 306–329.
[56] Goyal, D., and Pabla, B. S., 2015, "Condition Based Maintenance of Machine Tools–A Review," CIRP. J. Manuf. Sci. Technol., **10**, pp. 24–35.
[57] Doebling, S. W., Farrar, C. R., and Prime, M. B., 1998, "A Summary Review of Vibration-Based Damage Identification Methods," Shock Vib. Digest, **30**(2), pp. 91–105.
[58] Sarrafi, A., and Mao, Z., 2019, "Using 2D Phase-Based Motion Estimation and Video Magnification for Binary Damage Identification on a Wind Turbine Blade," Model Validation and Uncertainty Quantification, Vol. 3. Springer, pp. 145–151.
[59] Wadhwa, N., Rubinstein, M., Durand, F., and Freeman, W. T., 2013, "Phase-Based Video Motion Processing," ACM Trans. Graph. (TOG), **32**(4), p. 80.
[60] Fleet, D. J., and Jepson, A. D., 1990, "Computation of Component Image Velocity From Local Phase Information," Int. J. Comput. Vis., **5**(1), pp. 77–104.
[61] Choi, A. J., and Han, J. -H., 2018, "Frequency-Based Damage Detection in Cantilever Beam Using Vision-Based Monitoring System with Motion Magnification Technique," J. Intell. Mater. Syst. Struct., **29**(20), pp. 3923–3936.
[62] Yang, Y., Dorn, C., Mancini, T., Talken, Z., Theiler, J., Kenyon, G., Farrar, C., and Mascarenas, D., 2018, "Reference-Free Detection of Minute, Non-Visible, Damage Using Full-Field, High-Resolution Mode Shapes Output-Only Identified From Digital Videos of Structures," Struct. Health. Monit., **17**(3), pp. 514–531.
[63] Yang, Y., Dorn, C., Mancini, T., Talken, Z., Kenyon, G., Farrar, C., and Mascare nas, D., 2017, "Blind Identification of Full-Field Vibration Modes From Video Measurements with Phase-Based Video Motion Magnification," Mech. Syst. Signal Process., **85**, pp. 567–590.
[64] Chen, J. G., Wadhwa, N., Cha, Y. -J., Durand, F., Freeman, W. T., and Buyukozturk, O., 2015, "Modal Identification of Simple Structures with High-Speed Video Using Motion Magnification," J. Sound. Vib., **345**, pp. 58–71.
[65] Holzmond, O., and Li, X., 2017, "In Situ Real Time Defect Detection of 3D Printed Parts," Addit. Manuf., **17**, pp. 135–142.
[66] Straub, J., 2017, "Identifying Positioning-Based Attacks Against 3D Printed Objects and the 3D Printing Process," Pattern Recognition and Tracking XXVIII, Vol. 10203, International Society for Optics and Photonics, p. 1020304.
[67] Smith, J. O., 2007, *Mathematics of the Discrete Fourier Transform (DFT): With Audio Applications*, 2nd ed., W3K Publishing, http://www.w3k.org/books/.
[68] Gautama, T., and Van Hulle, M. A., 2002, "A Phase-Based Approach to the Estimation of the Optical Flow Field Using Spatial Filtering," IEEE Trans. Neural Netw., **13**(5), pp. 1127–1136.
[69] Liu, C., Torralba, A., Freeman, W. T., Durand, F., and Adelson, E. H., 2005, "Motion Magnification," ACM Trans. Graphics, **24**(3), pp. 519–526.
[70] ASTM International, 2015, *ASTM D638-14, Standard Test Method for Tensile Properties of Plastics*, ASTM International, West Conshohocken, PA.